On-Chip Metasurface-on-Facets for Ultra-High Transmission through Waveguides in Near-Infrared

Eran Falek, Aviad Katiyi, Yakov Greenberg, and Alina Karabchevsky*

Nature has long inspired scientists and engineers to develop transparent surfaces via constructing anti-reflective surfaces. In absence of anti-reflection (AR) coating, silicon reflects about 35% of light for a single interface air–silicon. Here, inspired by jellyfish anti-reflective eyes, a man-made anti-reflective surface on the facet of the waveguide is proposed and demonstrated for waveguides transparency in near-infrared. The optimized metamaterial with unit cells of 560×560 nm shows transparency of 2.6 times better as compared to the waveguide with blank facet. Metasurfaces are milled on the waveguides facets with a focused ion beam. Silicon-on-insulator waveguides are tested with an inline set-up. Far-field scattering diagrams reveal that it is the special geometry of the unit cells of the engraved metamaterial, which can be associated with the directional scattering resulting in combined effect: on one hand the ultra-high transparency of the device and on the other hand the efficient coupling to the low-order modes due to the focusing dielectric nano-antennas effect. Reported here waveguide facets as AR metamaterials on a chip, opens up opportunities to engineer transparent on-chip devices with high coupling efficiency for diverse applications from sensing to quantum technologies.

1. Introduction

On-chip photonics is a very promising compact platform to realize optical devices.[1] A single chip can include up to several hundred optical waveguides for a variety of applications such as on-chip laser, filters, light sources, amplifiers, and others.[1] Optical transparency is an essential characteristic of a waveguide's functionality and a measure of the transmitted power collected from the waveguide's distal end in comparison to power arriving at its input. The transmission efficiency is affected by the propagation losses, coupling efficiency, but mostly humbled, by the Fresnel reflections from the input and output facets. Due to their compatibility to CMOS technology, high-index core waveguides made of high-index semiconductor materials, such as silicon and gallium arsenide, are commonly used in optical communications,[2] as interconnec-

tors and biosensors[3] to switching,[4] multiplexing, division, and mode conversion.[1] However, due to the high refractive index of the semiconductor core materials,[5] they inherent inevitable reflection losses resulting in low transmission efficiency. In silicon, for instance, the reflection can be as high as 35% from the single facet air-silicon.[6]

The anti-reflection (AR) phenomena on a surface were first noticed by Lord Rayleigh in 19th century. He observed that a tarnished piece of glass exhibited an increase in light transmission. Lord Rayleigh explained that an AR coating on the glass is realized due to the gradual change in the refractive index from the lower-index medium to higher-index medium.[7–9] In later work by Bauer in 1934, the idea of engineering a dielectric coating to decrease reflectance from a substrate was proposed.[10] To treat the reflections, optical coatings[11,12] and metasurfaces exhibiting anti-reflective properties[6,13,14] were proposed. Numerous anti-reflection (AR) coatings have been developed which can be roughly divided into two categories: layered structures and nanostructure-based coatings.[15] The layered medium category includes the well-known quarter-wave transformer,[9] as well as multilayers structures such as the V- and W- type coatings,[16,17] and proprietary commercial coating such as the Conturan (commonly used in displays) and Amiran.[18] These methods are based on creating destructive interference between the incident and the refracted light. Despite their effectiveness, these methods tend to be band-limited. Another type of multilayer coating method is the gradient refractive index (GRIN) profile as shown in **Figure** 1d. The substrate is coated with multiple layers to increase the refractive index from air toward the substrate.[19] GRIN-based coatings can operate in a broad spectral range. Traditional multilayer-based AR coatings suffer from several limitations, such as material selection, fabrication costs, angular and spectral dependence. In addition, since the facet of a waveguide is in order of microns, deposition of multiple layers over them is not practical. To overcome these limitations, the second category of AR coating can be used, which includes porous materials[20,21] and sub-wavelength structures (SWS). SWS are an array of nanostructures, where the unit-cell is much smaller than a wavelength, which behaves microscopically as an effective equivalent medium.[22] Using those structures the scattered wave can be controlled to achieve

Dr. E. Falek, A. Katiyi, Y. Greenberg, Dr. A. Karabchevsky
School of Electrical and Computer Engineering
Ilse Katz Institute for Nanoscale Science and Technology
Ben-Gurion University of the Negev
Beer-Sheva 8410501, Israel
E-mail: alinak@bgu.ac.il

The ORCID identification number(s) for the author(s) of this article can be found under https://doi.org/10.1002/adom.202100130.
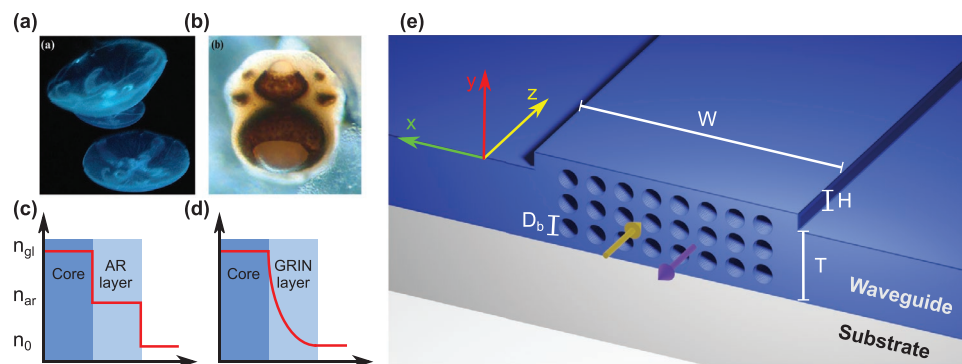
Figure 1. a) Jellyfish in an aquarium (Reproduced from[10]. Copyright 2018, Wiley-VCH). b) The eyes of the box jellyfish, *Tripedalia cystophora* (Reproduced with permission.[43] Copyright 2005, Springer Nature). The refractive index change of c) an AR coating and d) a GRIN coating. e) illustration of the metasurface engraved on the rib waveguide facet experiencing the anti-reflective properties.

transparency[23–25] and as nanoantenna for mode-selective polarization (de)multiplexing.[26,27] However, most of the metasurfaces are resonative arrays of nanoantennas and therefore they exhibit a narrow bandwidth behavior. One of the SWSs which experiences the broadband behavior is based on the "moth-eye"-like structure.[28–30] The "moth-eye" pattern consists of the cone-shaped unit-cells which effectively create a gradient index profile. Thus, such a non-resonant structure can be engraved from the device material, without additional fabrication consuming coatings.

Over the past 15 years, there has been a growing interest in tackling reflection from the facets of optical waveguides. In 2007, a subwavelength grating on the facet of a silicon-on-insulator waveguide was suggested to reduce reflections by the means of gradient index effect.[14] The reflections were reduced to 2% and 2.4% for the fundamental TE and TM modes, respectively. Etching the waveguide facet was also used to improve the reflections[31] and as subwavelength index matching structure for grating based couplers.[32] Similar methods were also employed for longer wavelengths. For example, anti-reflective structures were fabricated by etching diamond microstructure to achieve average transmission of 96.4% in the region of 10–50 μm.[33] Different emerging techniques to improve transmission involve employing advanced materials. Estakhri et al. suggested using subwavelength structures of combined electric and magnetic materials which together satisfy a self-duality condition.[13] This condition is sufficient to ensure 100% transmission that is robust to the presence of discontinuities along the propagation path. Exploiting photonic doping technique was suggested to achieve materials with near-zero permittivity and tunable permeability.[34] Such a region behaves as a lumped reactive element that can be used to design impedance matching network suitable for operation in a wide range: from radio frequency (RF) to optical applications. Periodic subwavelength structures on waveguides can also be used to give the waveguide another functionality. For example, subwavelength grating on a waveguide was used to create a broadband TE polarizer with high extinction ratio.[35] Other applications also exist, such as filter, mode converters, multiplexers, and couplers.[36–39]

Here, inspired by the eyes of the box jellyfish (Figure 1a), *Tripedalia Cystophora* which have a unique natural structure

of a GRIN with a central refractive index of 1.48 to reduces the reflection (Figure 1b), we design the AR metasurface on waveguide facet. In our previous work, we found that the transparency of optical multimode waveguides can reach more than 98% in a broad spectral range using properly designed metasurfaces engraved on a waveguide facet.[6] However, those predictions were never realised and tested. Here, based on the general theory developed in ref. [6], we obtain the optimal structure parameters which are suitable for fabrication, and for the first time test the fabricated waveguides. Based on the general theory developed in previous work,[6] we obtain the pattern and optimal parameters, fabricate and test the waveguides. For this, we apply the gradient index approach to increase the refractive index of the facet in a controlled manner. The AR metasurfaces are engraved on input and output waveguide facets in a periodic manner and consist of parabolic inclusions, as shown in Figure 1e. As compared to high quality factor dielectric gradient index metasurfaces,[40] here we aim to obtain broad spectrum performance of proposed metasurface-on-facet. We report on metasurface on waveguide facet acting as the near-IR AR structure resulting in waveguide transparency effect 2.21 times higher as compared to untreated waveguide facets.

2. Results and Discussion

Here, we study anti-reflective (AR) structures to minimize the reflection from facets of a silicon-on-insulator (SOI) rib waveguide shown in Figure 1e. For this, we designed the AR structures as a metasurface; a subwavelength periodic structure that allows controlling the effective refractive index of the core material. The metasurface is composed of a 2D array of parabolic inclusions as shown in Figure 1e, which creates a GRIN change from air to the waveguide material. The GRIN minimizes the reflection by reducing the Fresnel reflection. We design the metasurface to modify the effective refractive index of the waveguide by changing the ratio between the air (medium of the inclusion) and the waveguide core material by using Rytov's formula[41]:

$$n_{eff}^2 \cong f n_a^2 + (1-f) n_g^2 \qquad (1)$$

where $f = A_{air}/A_u$ is the fill factor, n_a is the refractive index of the inclusion (in our case a paraboloid made of air), and n_g is the refractive index of the ambient material (silicon in our case). Equation (1) is an approximation that is valid as long as the unit cell is significantly smaller than λ/n_s. For discussion on the size limitation of Equation (1) we refer the reader to ref. [42]. However, even if we take a rigorous approach to extract the required shape, the physics behind the AR mechanism still stems from the gradient index approach. The gradient may vary, but still gradually from close to index of 1, and up to the refractive index of silicon. This is because the parabolic shape of the studied features was reported in our recent theoretical paper.[6]

The result of applying Equation (1) to the parabolic inclusions array is that on the waveguide facet (the base of the unit cell) the effective refractive index is close to that of air, while it increases gradually as the light propagates deeper into the waveguide. At the paraboloids tip, the effective refractive index is that of silicon.

First, we estimate the transmission enhancement in presence of the AR metasurface analytically utilizing M-layers formalism[44] when the metasurface is divided into equal layers as illustrated in **Figure 2**a. Each layer is given by the effective refractive index according to Equation (1). For N layers, we relate the fields in the first and last media of layers via the matrix multiplication

$$\mathbf{E}^N = \mathbf{M}^N \mathbf{P}^{N-1} \mathbf{M}^{N-1} \mathbf{P}^{N-2} \cdots \mathbf{P}^1 \mathbf{M}^1 \mathbf{E}^1 = \mathbf{M}^t \mathbf{E}^1 \tag{2}$$

where $\mathbf{P}^i$ are the propagation matrices in the ith layer, given by

$$\mathbf{P}^i = \begin{pmatrix} e^{-jk_0 n^i \cos\theta_i \Delta_z} & 0 \\ 0 & e^{jk_0 n^i \cos\theta_i \Delta_z} \end{pmatrix} \tag{3}$$

Here $k_0 = \omega/c_0$ is the wave number in vacuum, n_i is the effective refractive index of the i-th layer, θ_i is the angle of propagation in the i-th layer and Δ_z is the layer's thickness.

At the interface between layers, the fields are related by M^i and the use of reflection coefficients depending on light polarization. The electric fields at the interface follow

$$\begin{pmatrix} E_r^2 \\ E_l^2 \end{pmatrix} = \begin{pmatrix} M_{11} & M_{12} \\ M_{21} & M_{22} \end{pmatrix} \begin{pmatrix} E_r^1 \\ E_l^1 \end{pmatrix} \tag{4}$$

and

$$M_{11} = M_{22} = \frac{1}{1-r} \tag{5a}$$

$$M_{12} = M_{21} = \frac{r}{r-1} \tag{5b}$$

where reflection coefficient r is either r_{TE} or r_{TM} which are related to reflection for TE or TM polarizations respectively. The reflection coefficients are given by

$$r_{TE} = \frac{n_i \cos\theta_i - n_{i+1}\cos\theta_{i+1}}{n_i \cos\theta_i + n_{i+1}\cos\theta_{i+1}} \tag{6a}$$

$$r_{TM} = \frac{n_i \cos\theta_{i+1} - n_{i+1}\cos\theta_i}{n_i \cos\theta_{i+1} + n_{i+1}\cos\theta_i} \tag{6b}$$

Here, n_i and n_{i+1} are the refractive indices of the the medium before and after the interface, and θ_i and θ_{i+1} are the angle of propagation in the layers i and $i + 1$, respectively.

By finding the system transfer matrix $\mathbf{M}^t$, the total structure reflection and transmission coefficients are given by

$$R = \left| \frac{M_{21}^t}{M_{11}^t} \right|^2 \tag{7a}$$

$$T_{TE} = \left| M_{11}^t - \frac{M_{21}^t}{M_{11}^t} \right|^2 \tag{7b}$$

$$T_{TM} = \left(\frac{\cos\theta_{in}}{\cos\theta_{out}} \right)^2 \left| M_{11}^t - \frac{M_{21}^t}{M_{11}^t} \right|^2 \tag{7c}$$
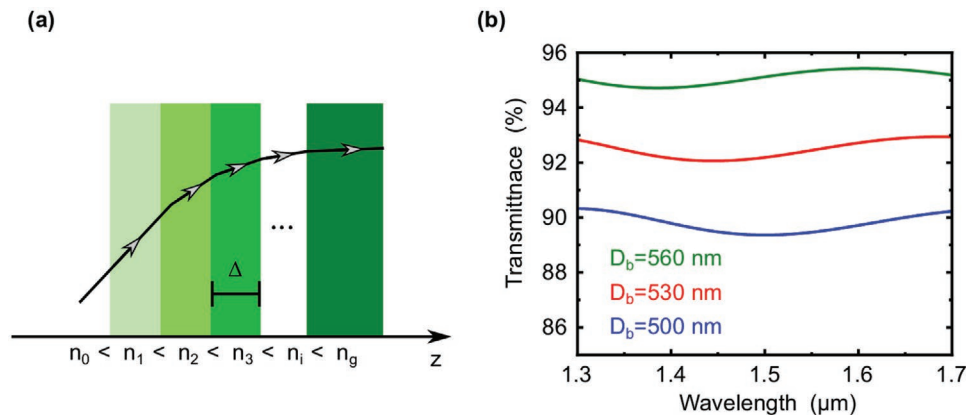

Figure 2. Schematics of gradient index profile layers on waveguide facet. a) Illustration of the ray trajectory due to the variation of the refractive index. b) A simulation of a layered medium based on parabolic inclusions of depth $H = 900$ nm and base diameter of $D_b = 500, 530, 560$ nm in a unit cell size of 560×560 nm.

The influence of different unit cells on the reflection of a layer consisting of the waveguide facet can be found in ref. [6]. Here, using the *M*-layer method, we calculate the transmittance for a different base diameter of the paraboloid for a unit cell size of 560×560 nm. The results are shown in Figure 2b. As the base diameter of the paraboloid increases, the effective refractive index approach $n = 1$ (air) resulting in improved transmission for larger base diameters. Higher transmission can be also achieved by reducing the unit cell size as was shown in ref. [6]. However, the fabrication of parabolic inclusions with a smaller diameter is much more challenging and will restrict the depth of the inclusion to roughly twice the diameter. This limitation on the depth or the thickness of the gradient index layer responsible for sharper gradient, and therefore, is less effective in reducing reflections. In addition, the AR structure acts as broadband behavior of the gradient index structure as shown in Figure 2b.

To further expand on the physics behind the transmission improvement of the array with a unit cell of parabolic shape, a far-field scattering pattern simulation was performed. We investigated the scattering far-field patterns from a single parabolic inclusion surrounded by silicon when the incident light is a plane wave. The incident light illuminates the base (**Figure 3**a) or the tip (Figure 3b) of the parabolic inclusion. The far-field scattering patterns are shown in Figure 3c,d. The far-field scattering patterns show that the parabolic inclusion exhibits a very low backward scattering intensity of the incidence light. Therefore, the unit cell of parabolic shape inclusion was chosen to study the

anti-reflection effect on our waveguide facets. Here we report on the single particle far-field scattering in addition to the previously reported by us the collective effect using periodic boundary in ref. [6]. The far-field simulation raises an important issue, which is even without the collective effect of the array and the gradient approach, the shape of the unit cell has low reflections and this may further improve the efficiency of the power transfer.

Next, we studied the AR metasurface on a multimode SOI rib waveguide for studying the effect of the collective response of an array of inclusions. The waveguide was simulated using finite difference time domain (FDTD) numerical simulation and validated with CST software. The dimensions of the silicon waveguide were set to thickness of $T = 1.6$ μm, strip height of $H = 0.4$ μm with width of $W = 6.2$ μm as shown in Figure 1e. The AR metasurface array consists of three rows and 11 columns with a unit-cell (size of 560×560 nm) of parabolic inclusion. The Gaussian beam polarized in y direction (TM) with a minimum diameter of 6 μm is launched onto the waveguides. The source plane was located at a distance of 1.5 μm from the input facet and focused at the center of the facet. The electric field at the cross-section in the yz plane for waveguides with and without AR metasurface is shown in **Figure 4**a,b. From the interference pattern shown in the field distribution of Figure 4b, we learn that the light is confined in the waveguide core in case the waveguide facet has AR metasurfaces design which we report here.

To calculate the transmission coefficient, we evaluated the reflected and the coupled power. To obtain the reflected power, we integrated the power flow on the entire plane located at
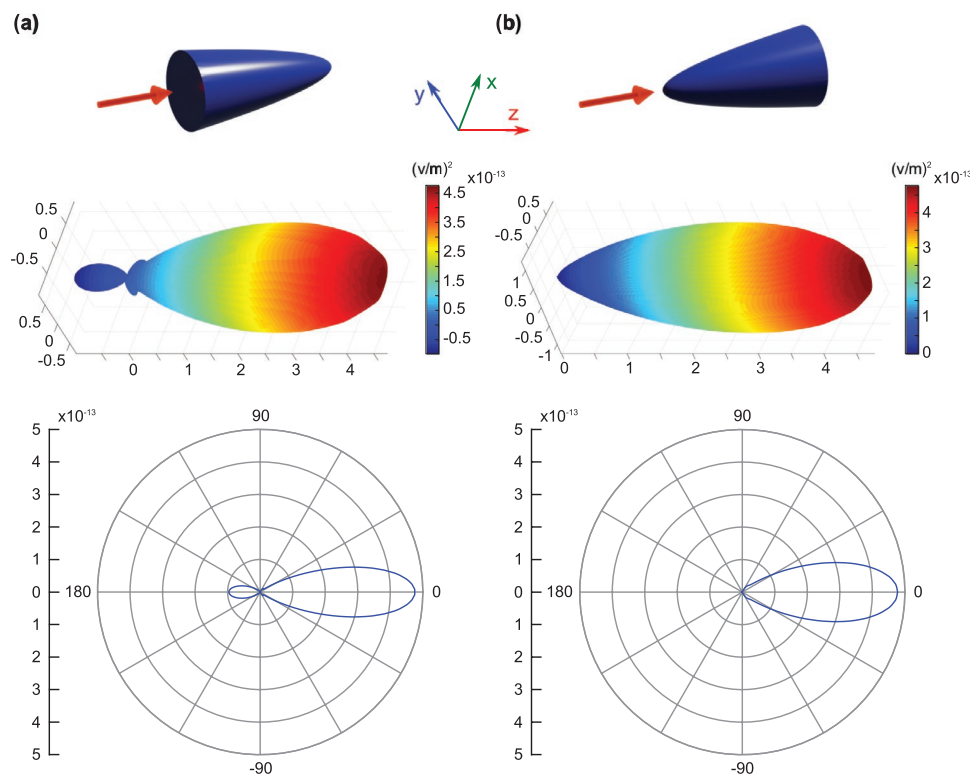

Figure 3. A far field scattering of a plane wave from a single parabolic inclusion embedded silicon. a) 3D linear radiation pattern (top) and polar radiation pattern (bottom) from unit cell illuminated from the basis. b) 3D linear radiation pattern (top) and polar radiation pattern (bottom) from unit cell illuminated from the tip. Note: Polar plot of the radiation pattern for $\phi = 0$.
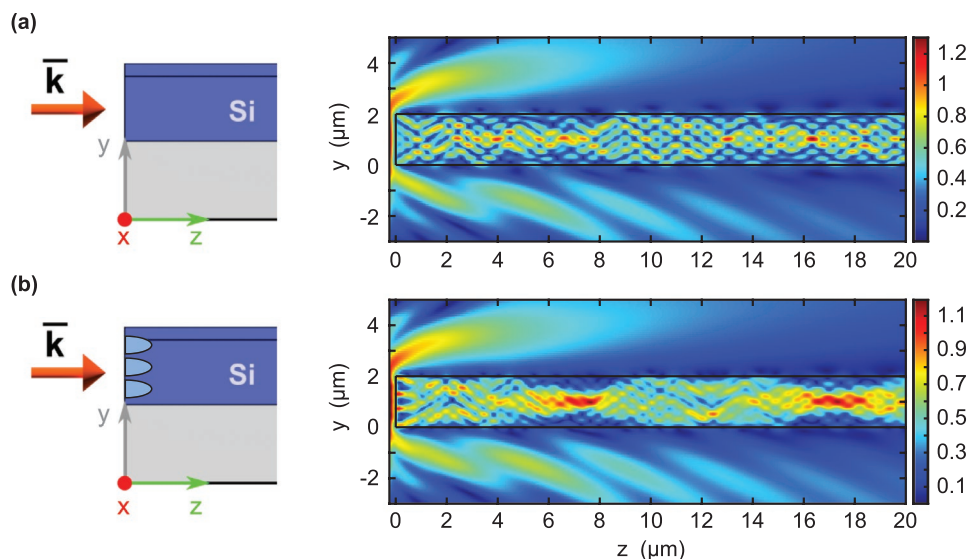
ADVANCED
SCIENCE NEWS
www.advancedsciencenews.com

ADVANCED
OPTICAL
MATERIALS
www.advopticalmat.de

Figure 4. Simulation results. Calculated cross-section of TM modes in *xz* plane of studied waveguides with a) smooth facet and with b) the anti-reflection metasurface-on-facet.

1 µm behind the source and obtained P_{ref}. To obtain the coupled power, we integrated the power flow at two planes ($z = 10$, 12 µm) along the waveguide for the entire waveguide cross-section. The results were averaged to obtain the coupled power P_c. The coupled power was chosen for the power normalization because the Gaussian beam shape is circular while the waveguide facet is rectangular. Since the excitation includes the facet area, there is a large portion of the beam that propagate outside the waveguide. Therefore, in the case of normalization to the total beam power, the transmission would be very low due to the lack of coupling mechanism rather than reflections. We focus on reducing reflections and therefore only the power interacting with the facet is considered. The transmission coefficient for a single facet was calculated with

$$T_{sf} = \frac{P_c}{P_c + P_{ref}} \quad (8)$$

We observed a maximum transmission improvement of 21%, while the transmission with the AR structures is as high as up to 88% (shown in the Supporting Information). Based on the analytical calculation presented in Figure 2, we achieved transmission of 95% for the given parameters of the unit cells of paraboloidal shape.

To explore the anti-reflection effect of the metasurface on the facet, we fabricated a SOI rib waveguide with slab height of 1.6 µm, strip height of 0.4 µm (Figure 1a) with varying strip width. The inclusions were fabricated on waveguide facets using a focused ion beam (FIB) on waveguides. **Figure 5**a shows the scanning electron microscopy (SEM) image of a reference waveguide and a waveguide with the anti-reflection metasurface. Figure 5b shows an SEM image of the facet of the fabricated waveguides with the anti-reflection metasurface with a diameter of 530 nm and height of 900 nm of each unit cell.

We constructed the experimental setup shown in **Figure 6**a. A broadband laser source was coupled into a single-mode fiber

using an X10 focusing objective. To minimize the spot size of the laser on the waveguide facet, the single-mode fiber was connected to a lensed-fiber by FC/PC connector. The lensed-fiber was aligned to the waveguide using a 3D stage and monitored by a microscope for precise coupling. The output signal was collected using a single-mode fiber into a spectrum analyzer. Figure 6c,d shows the coupling to the waveguide input and output facet. First, we measured the power transmission on a reference waveguide with a width of 6.2 µm and without inclusions and aligned the fiber for maximum transmission. Next, we shifted the fiber to an adjacent waveguide with metasurface anti-reflection structures, as can be seen in Figure 5. Figure 6b shows the experimental results of a reference waveguide and a waveguide with the AR structure.

We achieved an enhancement of 221% in the transmitted power when both input and output facets were sculptured with engraved AR metasurfaces as compared the reference. Figure 6b shows the transmission of the waveguide with the AR structure and the reference waveguide. According to the simulation, the transmission through a single facet is more than 70% all through the spectrum, which is simply more than 49% for two facets. Therefore, as long as the waveguide itself is passive, one cannot have an improvement of more than 100% due to the energy
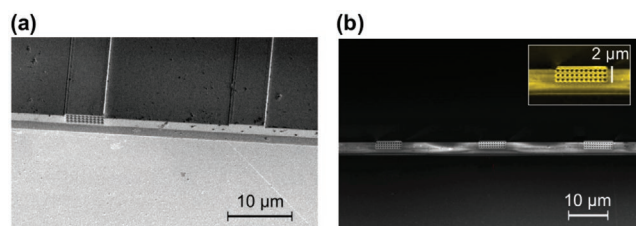

Figure 5. Scanning electron micrography (SEM) images of a) the waveguide with inclusions, the reference waveguide and b) the input facet of the fabricated waveguides with enlarged SEM image of the fabricated structure.
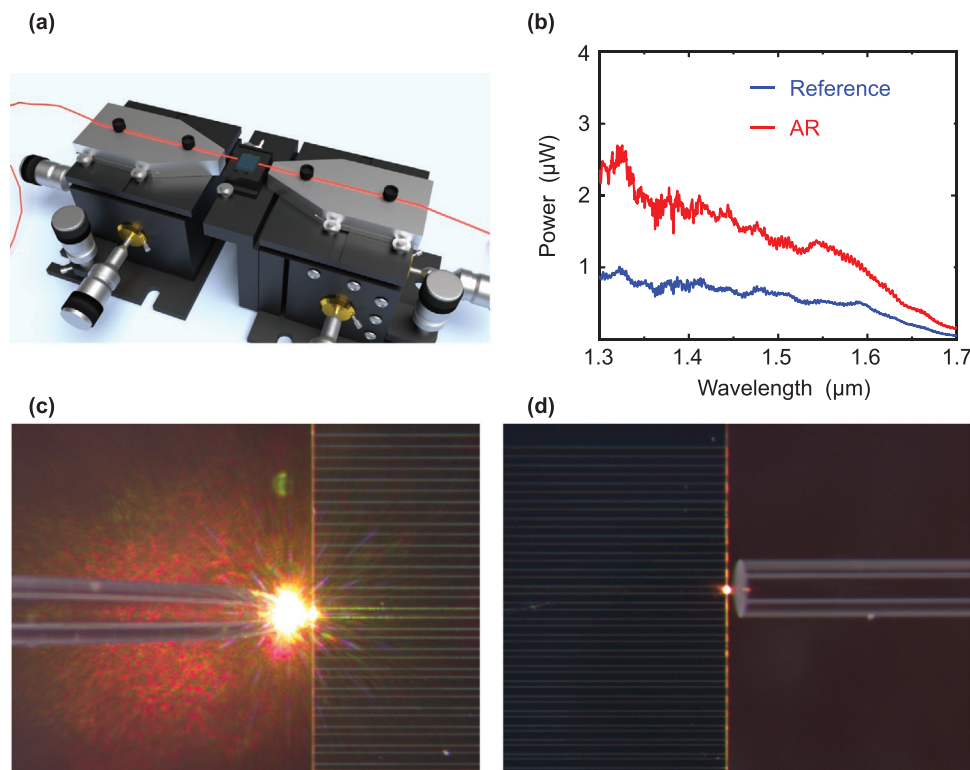
Figure 6. a) Experimental setup. b) The experimental results of a reference waveguide (blue curve) and a waveguide with the anti-reflection (AR) structure (red curve). c) Coupling to the input facet. d) Collecting from the output facet.

conservation. From the extraordinary improvement during the experimental validation as compared to the numerical predictions, we learned that such a transmission is a combined effect of reflection suppression and focusing into the facet resulting in improved coupling efficiency, the waveguide numerical aperture. In the simulation, the transmission was calculated compared to the power approaching the facet. However, in the experiment, the transmission power is also affected by the above mentioned factors, and therefore, the actual transmission of a reference waveguide may be low enough to allow improvement of 221%. Figure 6b shows a bandwidth of 400 nm from 1300 to 1700 nm. Two factors define the bandwidth of the AR structure. For shorter wavelengths, the diameter of the inclusions (and hence, the unit-cell size) should be sub-wavelength. When this term violates the efficiency of the AR structure decreases. In the simulation that happened at 1300 nm, as well as in the experimental result. Therefore, based on the experimental data, the approximate coupling bandwidth of the reported by us device is 1300 to 1700 nm. However, we still had transmission improvement even down to 1100 nm. For the longer wavelength, the thickness of the AR layer (i.e., H) determines the slope of the gradient. One can increase the bandwidth by using deeper holes, however, there is a fabrication limitation on the ratio between the diameter and the depth.

3. Conclusion

In conclusion, we reported on anti-reflective metasurfaces engraved on silicon waveguide facets. The unit cell of each metasurface is in shape of paraboloidal inclusions experiencing directional forward scattering effect. The suggested structure behaves effectively as a gradient index matching layer, which reduces the Fresnel reflection in broad spectral range for different incident angles. We optimized the size of the unit-cells as well as the inclusion dimensions before the fabrication with FIB. The FIB process may cause iron doping on the surface of the facet, which in turn may introduce additional losses. The presence of potential losses in the engraved structures will behave as resonators confining light and may add to the aforementioned loss. However, from the analysis of the experimental measurements we learn that if those losses exist, their effect is negligible. Therefore, the effect of potential losses induced by FIB process was not added to our numerical model. The resulted structures were analyzed with M-layers semi-analytical calculation and with FDTD to determine the actual effect for a waveguide facet. The numerical simulation showed an improvement of up to 21.5% compared to the transmission without AR structures for a single facet. Far-field scattering simulation of the unit cells was also performed, showing suppressed back-scattering and directional forward scattering. Fabricated AR-metasurfaces on waveguide facets were tested with an inline home-made set-up. The experimental results showed an improvement of up to 2.21 times in the transmitted power for the treated waveguide as compared to the reference waveguide. An improvement of over 100% implies that the structures were efficient in improving other possible factors, such as coupling efficiency, waveguide numerical aperture, and the distribution of the modes. However, these factors are out of the

**ADVANCED
SCIENCE NEWS**

www.advancedsciencenews.com

**ADVANCED
OPTICAL
MATERIALS**

www.advopticalmat.de

scope of the current paper. These results seem promising for enhancing the transmission efficiency for CMOS-compatible high-dielectric waveguide applications.

4. Experimental Section

Numerical Simulation: To assess the transmission improvement, a FDTD simulation was performed using the CST Studio Suite which is a high-performance 3D EM analysis software package for designing, analyzing, and optimizing electromagnetic (EM) components and systems. The structure is a rib waveguide, with a rib height $H = 400$ nm, which is extruded from a layer with a thickness of $T = 1600$ nm. The rib width is $W = 6196$ nm, it is made of silicon, and is deposited over a thick substrate of silica. Two structures are compared. One is a waveguide without anything on the facets, for reference. The other is a similar waveguide, where an array of 3×11 paraboloids, with base diameter $D_b = 500$ nm and depth of 900 nm was drilled on the input and output facet surfaces. Since the studied waveguide is long, the simulation was divided into three steps. In the first step, the structure length along the z direction was set to 18 µm and was terminated by an open boundary condition (BC), which emulates a half infinite waveguide. This structure was exited using a Gaussian beam with a minimum diameter of 6 µm which focuses at a distance of 1.5 µm from the source surface. The focal point of the beam was located at the center of the facet, that is, at $(x, y) = (0, 1)$ µm. The purpose of the first step was to calculate the power going into the waveguide after the first facet, as well as the total power arriving at the facet. Since the structure was a multi-mode waveguide, the simulation exhibit some variation in the power flowing in the waveguide for different locations along the waveguide. For this reason, the power in the waveguide was integrated at four different distances and averaged. The measurement locations are $z = 10$ µm and $z = 12$ µm. The reflected power was also calculated at a surface located at 1 µm behind the source. Since the source plane excited the Gaussian beam only at the $+z$ direction, the fields behind the plane were exclusively the result of the reflection from the waveguide. After integrating over the reflected power, the total power arriving the facet was calculated as $P_t = P_{in} + P_{ref}$.

Waveguide Fabrication: The rib waveguide (as detailed in ref. [3]) was fabricated on SOI wafer with silicon carrier, 2 µm silica SiO_2 and 2 µm of silicon. To write the waveguides the e-beam resist poly-methyl methacrylate (PMMA) 950 K was used. Once the PMMA resist was developed, aluminum was evaporated to serve as a hard mask with a thickness of 50 nm via an electron gun evaporator. Next, the chip in acetone was soaked for 4 h (lift-off process) and cleaned the chip with isopropanol. Eventually, the chip was dry etched with SF_6 + Ar and O_2 to achieve straight lines and 90° waveguide walls. The residue of the Al hard-mask was removed with a 400 K developer.

Metasurface-on-Facet Fabrication: The metasurfaces were engraved on waveguides facets with a focused ion beam milling machine.

Experimental Setup: To perform the experiments we launched the broadband laser source (Fianium WL-SC-400-15) was launched with a bandwidth of 450–2400 nm into single-mode fiber (1550BHP) using an X10 plan achromatic objective (Olympus) with a numerical aperture of NA = 0.25. The single-mode fiber was connected to the lensed-fiber through FC/PC connector. The lensed-fiber was coupled to the waveguide via fine alignment using a 3D stage (3-Axis NanoMax Stage). To better calibrate and for precise alignment the waveguide lines were imaged by stereo microscope (Zeiss Stemi SV6). The transmitted spectra were collected using a single-mode fiber connected directly into an optical spectrum analyzer (Yokogawa 6370D). The spectra were recorded at wavelengths of 1.3–1.7 µm with a resolution of 1 nm.

Supporting Information

Supporting Information is available from the Wiley Online Library or from the author.

Conflict of Interest

The authors declare no conflict of interest.

Data Availability Statement

The data that support the findings of this study are available from the corresponding author upon reasonable request.

[1] A. Karabchevsky, A. Katiyi, A. S. Ang, A. Hazan, *Nanophotonics* **2020**, *9*, 3733.

[2] E. J. Murphy, *Integrated Optical Circuits and Components: Design and Applications*, CRC Press, Boca Raton, FL **2020**.

[3] A. Katiyi, A. Karabchevsky, *ACS Sens.* **2018**, *3*, 618.

[4] A. Karabchevsky, A. Hazan, A. Dubavik, *Adv. Opt. Mater.* **2020**, *8*, 2000769.

[5] Z. Wang, A. Abbasi, U. Dave, A. De Groote, S. Kumari, B. Kunert, C. Merckling, M. Pantouvaki, Y. Shi, B. Tian, K. Van Gasse, J. Verbist, R. Wang, W. Xie, J. Zhang, Y. Zhu, J. Bauwelinck, X. Yin, Z. Hens, J. Van Campenhout, B. Kuyken, R. Baets, G. Morthier, D. Van Thourhout, G. Roelkens, *Laser Photonics Rev.* **2017**, *11*, 1700063.

[6] A. Karabchevsky, E. Falek, Y. Greenberg, M. Elman, Y. Keren, I. Gurwich, *Nanoscale Adv.* **2020**, *2*, 2977.

[7] L. Rayleigh, *Proc. London Math. Soc.* **1879**, *1*, 51.

[8] R. Jacobsson, J. O. Mårtensson, *Appl. Opt.* **1966**, *5*, 29.

[9] H. A. Macleod, *Thin-Film Optical Filters*, CRC Press, Boca Raton, FL **2017**.

[10] M. Motamedi, M. E. Warkiani, R. A. Taylor, *Adv. Opt. Mater.* **2018**, *6*, 1800091.

[11] H. K. Raut, V. A. Ganesh, A. S. Nair, S. Ramakrishna, *Energy Environ. Sci.* **2011**, *4*, 3779.

[12] B. Zhang, Y. Liu, Y. Luo, F. V. Kusmartsev, A. Kusmartseva, *Materials* **2020**, *13*, 5417.

[13] N. M. Estakhri, N. Engheta, R. Kastner, *Phys. Rev. Lett.* **2020**, *124*, 033901.

[14] J. Schmid, P. Cheben, S. Janz, J. Lapointe, E. Post, D.-X. Xu, *Opt. Lett.* **2007**, *32*, 1794.

[15] B.-T. Liu, W.-D. Yeh, *Thin Solid Films* **2010**, *518*, 6015.

[16] W. Glaubitt, P. Löbmann, *J. Eur. Ceram. Soc.* **2012**, *32*, 2995.

[17] J. Cox, G. Hass, A. Thelen, *JOSA* **1962**, *52*, 965.

[18] P. Löbmann, in *Chemical Solution Deposition of Functional Oxide Thin Films* (Eds: T. Schneller, R. Waser, M. Kosec, D. Payne), Springer, New York **2013**, pp. 707–724.

[19] G. Beadie, J. S. Shirk, A. Rosenberg, P. A. Lane, E. Fleet, A. Kamdar, Y. Jin, M. Ponting, T. Kazmierczak, Y. Yang, A. Hiltner, E. Baer, *Opt. Express* **2008**, *16*, 11540.

[20] H. K. Raut, S. S. Dinachali, K. K. Ansah-Antwi, V. A. Ganesh, S. Ramakrishna, *Nanotechnology* **2013**, *24*, 505201.

[21] H. J. Gwon, Y. Park, C. W. Moon, S. Nahm, S.-J. Yoon, S. Y. Kim, H. W. Jang, *Nano Res.* **2014**, *7*, 670.

[22] X. Luo, *Sci. China: Phys., Mech. Astron.* **2015**, *58*, 594201.

[23] B. Zhang, J. Hendrickson, N. Nader, H.-T. Chen, J. Guo, *Appl. Phys. Lett.* **2014**, *105*, 241113.

[24] M. K. Hedayati, M. Elbahri, *Materials* **2016**, *9*, 497.

[25] H.-T. Chen, J. Zhou, J. F. O'Hara, F. Chen, A. K. Azad, A. J. Taylor, *Phys. Rev. Lett.* **2010**, *105*, 073901.

[26] R. Guo, M. Decker, F. Setzpfandt, X. Gai, D.-Y. Choi, R. Kiselev, A. Chipouline, I. Staude, T. Pertsch, D. N. Neshev, Yuri S Kivshar, *Sci. Adv.* **2017**, *3*, e1700007.

[27] Y. Meng, Z. Liu, Z. Xie, R. Wang, T. Qi, F. Hu, H. Kim, Q. Xiao, X. Fu, Q. Wu, S.-H. Bae, M. Gong, X. Yuan, *Photonics Res.* **2020**, *8*, 564.

[28] G. D. Bernard, W. H. Miller, *Invest. Ophthalmol. Visual Sci.* **1968**, *7*, 416.

[29] J. Cai, L. Qi, *Mater. Horiz.* **2015**, *2*, 37.

[30] Z. Han, Z. Wang, X. Feng, B. Li, Z. Mu, J. Zhang, S. Niu, L. Ren, *Biosurf. Biotribol.* **2016**, *2*, 137.

[31] G.-R. Zhou, X. Li, N.-N. Feng, *IEEE J. Quantum Electron.* **2003**, *39*, 384.

[32] D. Benedikovic, C. Alonso-Ramos, P. Cheben, J. H. Schmid, S. Wang, D.-X. Xu, J. Lapointe, S. Janz, R. Halir, A. Ortega-Moñux, J. G. Wangemert-Pérez, I. Molina-Fernández, J.-M. Fédéli, L. Vivien, M. Dado, *Opt. Lett.* **2015**, *40*, 4190.

[33] P. Forsberg, M. Karlsson, *Opt. Express* **2013**, *21*, 2693.

[34] Z. Zhou, Y. Li, E. Nahvi, H. Li, Y. He, I. Liberal, N. Engheta, *Phys. Rev. Appl.* **2020**, *13*, 034005.

[35] Y. Xiong, D.-X. Xu, J. H. Schmid, P. Cheben, N. Y. Winnie, *IEEE Photonics J.* **2015**, *7*, 1.

[36] P. Cheben, P. J. Bock, J. H. Schmid, J. Lapointe, S. Janz, D.-X. Xu, A. Densmore, A. Delâge, B. Lamontagne, T. J. Hall, *Opt. Lett.* **2010**, *35*, 2526.

[37] P. Cheben, D. Xu, S. Janz, A. Densmore, *Opt. Express* **2006**, *14*, 4695.

[38] R. Halir, A. Maese-Novo, A. Ortega-Moñux, I. Molina-Fernández, J. Wangüemert-Pérez, P. Cheben, D.-X. Xu, J. Schmid, S. Janz, *Opt. Express* **2012**, *20*, 13470.

[39] R. Halir, P. J. Bock, P. Cheben, A. Ortega-Moñux, C. Alonso-Ramos, J. H. Schmid, J. Lapointe, D.-X. Xu, J. G. Wangüemert-Pérez, Í. Molina-Fernández, S. Janz, *Laser Photonics Rev.* **2015**, *9*, 25.

[40] M. Lawrence, D. R. Barton, J. Dixon, J.-H. Song, J. van de Groep, M. L. Brongersma, J. A. Dionne, *Nat. Nanotechnol.* **2020**, *15*, 956.

[41] S. Rytov, *Sov. Phys. JEPT* **1956**, *2*, 466.

[42] W. M. Wu, C. C. Njoku, W. Whittow, A. M. Zagoskin, F. Kusmartsev, J. Vardaxoglou, *J. Adv. Dielectr.* **2014**, *4*, 1450032.

[43] D.-E. Nilsson, L. Gislén, M. M. Coates, C. Skogh, A. Garm, *Nature* **2005**, *435*, 201.

[44] M. Born, E. Wolf, *Principles of Optics: Electromagnetic Theory of Propagation, Interference and Diffraction of Light*, Elsevier, New York **2013**.